Bioactive Materials 6 (2021) 1215–1222

Contents lists available at ScienceDirect

Bioactive Materials

journal homepage: www.sciencedirect.com/journal/bioactive-materials

Design and performance evaluation of additively manufactured composite lattice structures of commercially pure Ti (CP–Ti)

Wei Xu [a,b,c,1], Aihua Yu [a,1], Xin Lu [a,*], Maryam Tamaddon [b], Mengdi Wang [d], Jiazhen Zhang [a], Jianliang Zhang [e], Xuanhui Qu [a], Chaozong Liu [b], Bo Su [c]

[a] Beijing Advanced Innovation Center for Materials Genome Engineering, Institute for Advanced Materials and Technology, State Key Laboratory for Advanced Metals and Materials, University of Science and Technology Beijing, Beijing, 100083, China
[b] Institute of Orthopaedic & Musculoskeletal Science, University College London, Royal National Orthopaedic Hospital, Stanmore HA7 4LP, UK
[c] Bristol Dental School, University of Bristol, Bristol BS1 2LY, UK
[d] School of Physiology, Pharmacology and Neuroscience, University of Bristol, Bristol, BS8 1TD, UK
[e] School of Metallurgical and Ecological Engineering, University of Science and Technology Beijing, Beijing, 100083, China

ARTICLE INFO

Keywords:
Composite lattice structure
Finite element modelling
Selective laser melting (SLM)
CP-Ti

ABSTRACT

Ti alloys with lattice structures are garnering more and more attention in the field of bone repair or regeneration due to their superior structural, mechanical, and biological properties. In this study, six types of composite lattice structures with different strut radius that consist of simple cubic (structure A), body-centered cubic (structure B), and edge-centered cubic (structure C) unit cells are designed. The designed structures are firstly simulated and analysed by the finite element (FE) method. Commercially pure Ti (CP–Ti) lattice structures with optimized unit cells and strut radius are then fabricated by selective laser melting (SLM), and the dimensions, microtopography, and mechanical properties are characterised. The results show that among the six types of composite lattice structures, combined BA, CA, and CB structures exhibit smaller maximum von-Mises stress, indicating that these structures have higher strength. Based on the fitting curves of stress/specific surface area versus strut radius, the optimized strut radius of BA, CA, and CB structures is 0.28, 0.23, and 0.30 mm respectively. Their corresponding compressive yield strength and compressive modulus are 42.28, 30.11, and 176.96 MPa, and 4.13, 2.16, and 7.84 GPa, respectively. The CP-Ti with CB unit structure presents a similar strength and compressive modulus to the cortical bone, which makes it a potential candidate for subchondral bone restorations.

1. Introduction

Osteochondral defects can lead to mechanical instability of the joint and loss of joint function and can proceed to the generation of osteoarthritis (OA), which is one of the most prevalent joint diseases and a major cause of disability in the adult population [1]. In recent years, tissue engineering has emerged as a potential solution for the repair of damaged subchondral bone [2]. At present, metals, ceramics, and polymers have been used as subchondral scaffolds. Among them, metals especially Titanium (Ti) and its alloys scaffolds are widely used due to their high strength and fatigue resistance [3–6].

Porous Ti scaffolds are usually fabricated by conventional techniques, such as slurry foaming and space-holder method [7,8]. But these techniques have some limitations, for example, the shape, the size, and the distribution of pore are difficult to control accurately that leads to the expected performance cannot be achieved. Additive manufacturing (AM) is a new technology developed in recent years, which is defined as a process of joining materials to make objects from 3D model data, usually layer upon layer. With the development of additive manufacturing (AM) technology, scaffolds with unlimited arbitrary topological layouts, complex internal microstructures and particular properties (e.g. magnetic, excellent cell adhesion ability and mechanical properties) can be manufactured [9–11]. Among the additive manufacturing (AM) technology, such as selective laser sintering (SLS), electron beam melting (EBM), and selective laser melting (SLM), SLM is considered the most promising technology by which products are built by melting selected areas of powder layers under a protective atmosphere using a computer-controlled laser beam [12,13]. Compared with

* Corresponding author.
E-mail address: luxin@ustb.edu.cn (X. Lu).
[1] These authors contributed equally.

https://doi.org/10.1016/j.bioactmat.2020.10.005
Received 20 July 2020; Received in revised form 10 October 2020; Accepted 10 October 2020
Available online 7 November 2020

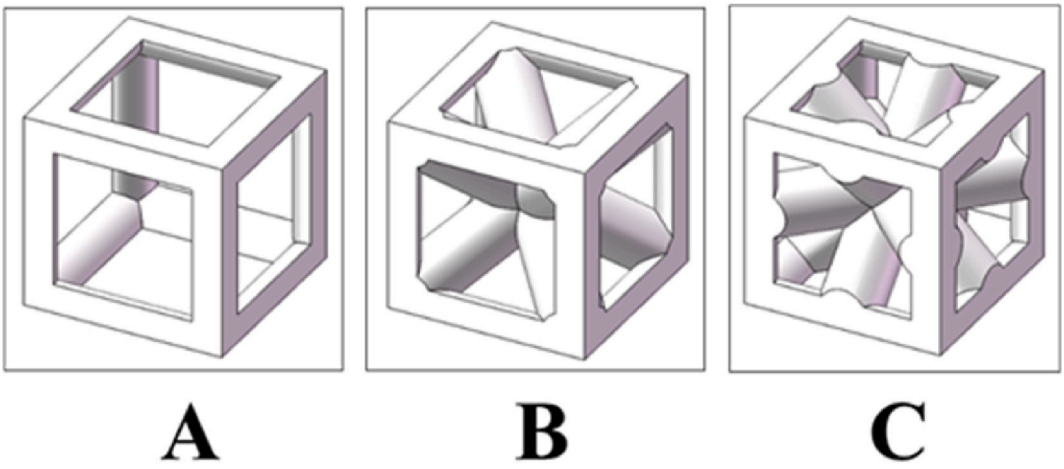

Fig. 1. The basic unit cells of A, B, C with the strut radius of 0.3 mm.

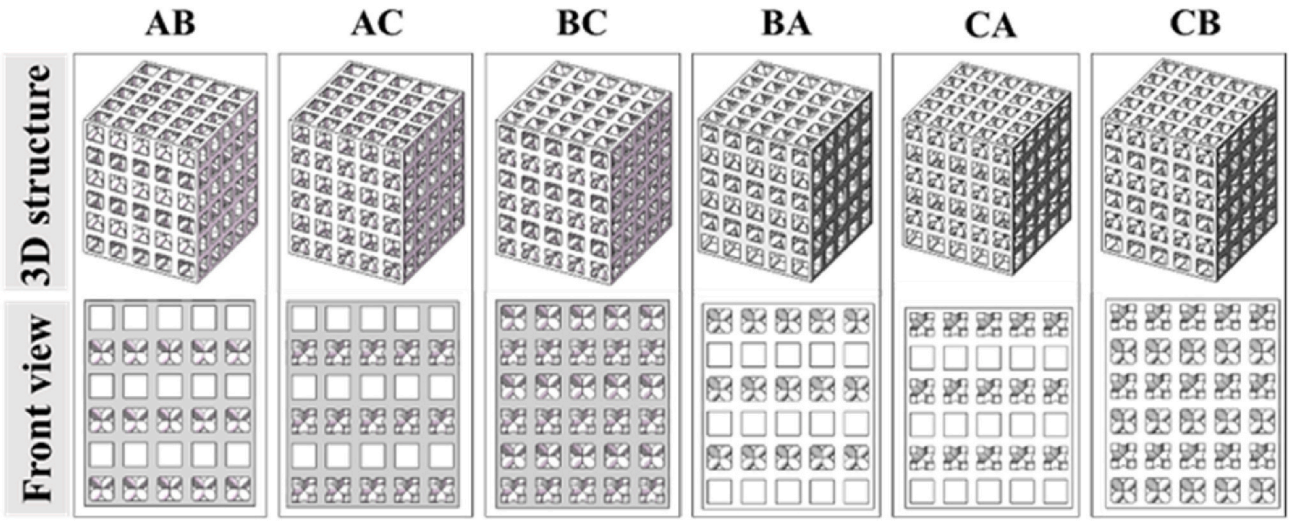

Fig. 2. The combined composite lattice structures and their front views.

conventional fabrication methods, SLM technology is more flexible in forming complex shapes, especially for scaffolds based on lattice structures [14,15].

So far, Ti scaffolds with different lattice structures, e.g. cubic or cubic-based lattices [16,17], diamond lattices [18,19], and gyroid lattices [20,21], have been fabricated by SLM. Such as Du et al. [22] designed uniform structures of 70% porosity with the unit cells of the cube, diamond, and Rhombic dodecahedron. The results showed that the compressive modulus was in the range of 25–120.4 GPa while the yield stress was more than 400 MPa. Although the compressive stress is higher than natural bone significantly that is enough for standing loads, the remarkably higher elastic modulus than that of bones will cause "stress shielding", which leads to bone resorption around the implants and ultimately the failure of implantation. In addition, Gyroid structures with the porosity of 70.99% ± 9.3% of Ti–6Al–4V alloy were fabricated by Zaharin et al. [23], and the results showed that the yield strength and compressive modulus were 22.44 ± 0.46 MPa and 10.6 ± 0.28 GPa, respectively. But these studies mainly focus on single lattice structures that cannot match the natural bones well at the strength and elastic modulus. Thus, from a design point of a view, it is imperative to design porous Ti scaffolds with different pore porosities and pore sizes, in order to match the mechanical and biological properties of natural bone [24–27].

Till now, there are some kinds of graded scaffolds have been fabricated by SLM to improve the mechanical and biological properties of the alloys [28–31]. Such as, Choy et al. designed and manufactured cubic lattice and honeycomb lattice structures with graded structure diameter and density, and the results demonstrated that the graded lattices performed better mechanical properties compared to uniform lattices. Zhang et al. manufactured a graded lattice structure based on diamond unit cells and it showed good mechanical properties and permeability. In order to enhance the mechanical and biological properties further, six types of composite lattice structures with different strut radius were designed in the present study. Then mechanical properties were investigated numerically using the FE method. Based on the simulated results, CP-Ti with optimized structures and strut radius were fabricated by SLM, and the morphology and compressive properties were characterised. It aims at designing the composite lattice structures and optimising the mechanical properties of CP-Ti, so as to provide basic guidance for its potential application in subchondral bone repair and restorations.

2. Materials and methods

2.1. Design of composite lattice structures

Three unit cells with a length of 2 mm, namely simple cubic (A), body-centered cubic (B), and edge-centered cubic (C), were designed by

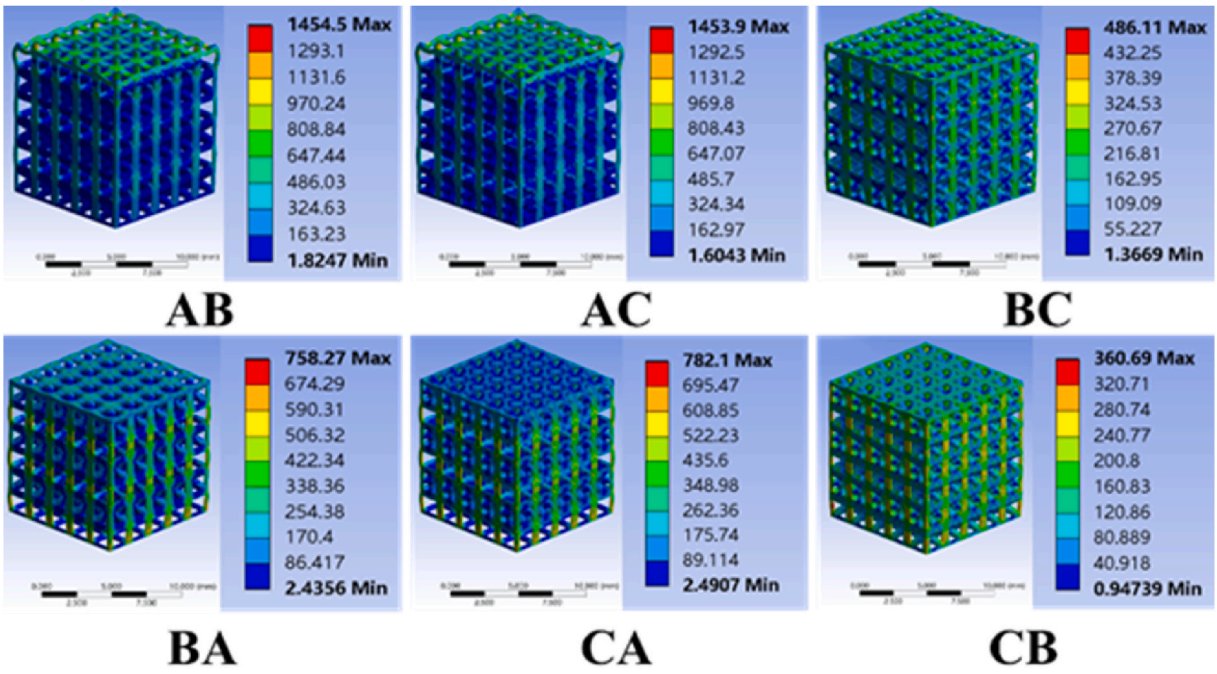

Fig. 3. Von-Mises stress distribution of composite lattice structures with strut radius of 0.3 mm.

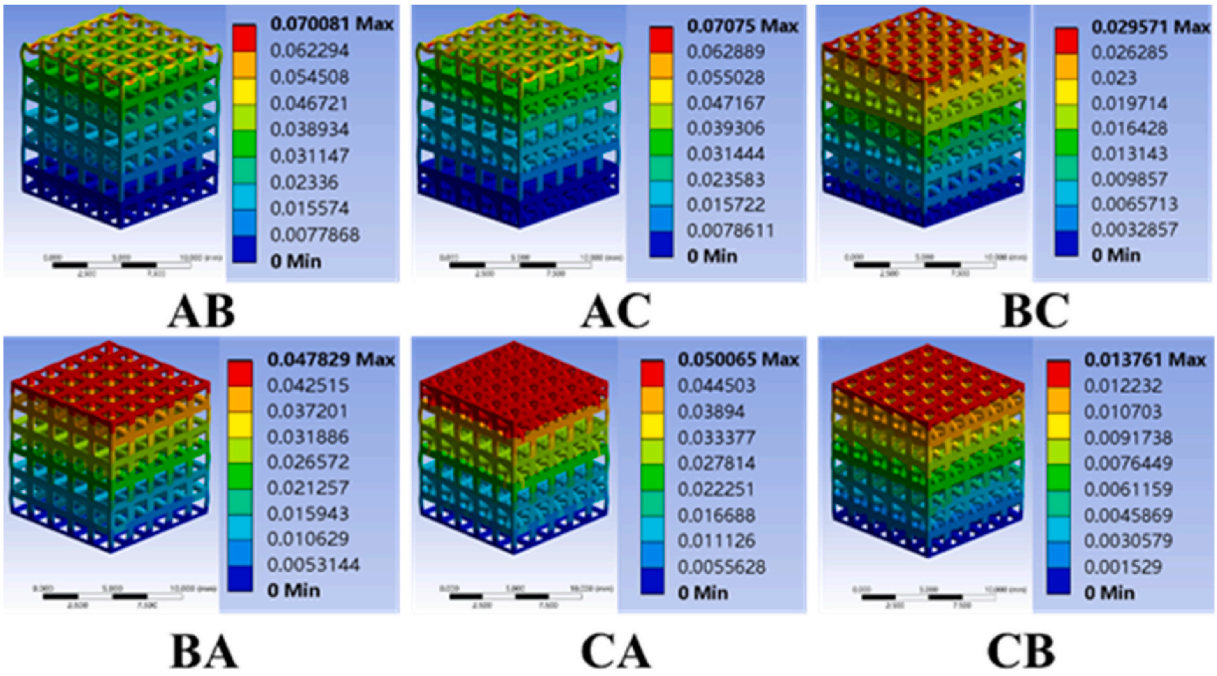

Fig. 4. Total deformation of composite lattice structures with strut radius of 0.3 mm.

the Solidworks software, as shown in Fig. 1. It is relatively easy to design these three unit cells due to their simple structures. Additionally, they could be manufactured well due to their relatively simple design and the significantly reduced warping effect caused by internal inclined struts during the SLM process. What's more, the inclined struts cross could reduce the flow velocity, which is beneficial for cell adhesion and proliferation. Six types of composite lattice structures were designed by the Solidworks software, i.e. AB, BA, AC, CA, BC, and CB structures. Due to the mechanical properties of lattice struts along different spatial directions are not the same and the direction of stress applied in the FEA simulations is from the top, the AB and BA structures are considered to be two different structures. The dimensions of samples were 10 × 10 × 12 mm (length × width × height) and the composite lattice structures were hybridized in the direction of the Z-axis by layering two different types of unit cell from top to bottom, e.g. AB lattice: A for the first, third and fifth layers and B with the same size for the second, fourth and sixth layers. The same design method was applied with BA, AC, CA, BC, and CB. For each composite lattice structure, different strut radius of 0.2, 0.25, 0.3, 0.35, and 0.4 mm were set, therefore a total of 30 different composite lattice structures were designed. Fig. 2 shows the six composite lattice structures with a strut radius of 0.3 mm and their front views.

Table 1
FE analysis results of composite lattice structures.

Model	Strut radius (mm)	Porosity (%)	Maximum total deformation (mm)	Maximum von-Mises stress (MPa)
AB	0.2	83.72	0.1667	3632.3
	0.25	76.13	0.1024	1956.1
	0.3	67.89	0.0701	1454.5
	0.35	59.37	0.0518	1018.7
	0.4	50.96	0.0397	776.4
BA	0.2	83.72	0.1011	1783.8
	0.25	76.13	0.0664	916.3
	0.3	67.89	0.0478	758.27
	0.35	59.37	0.0418	598.1
	0.4	50.96	0.0375	542.9
AC	0.2	82.01	0.1733	3675.0
	0.25	73.74	0.1064	1955.8
	0.3	64.87	0.0708	1453.9
	0.35	55.80	0.0528	1151.9
	0.4	47.07	0.0397	808.3
CA	0.2	82.01	0.0965	1208.1
	0.25	73.74	0.0670	896.2
	0.3	64.87	0.0501	782.1
	0.35	55.80	0.0372	625.3
	0.4	47.07	0.0312	596.6
BC	0.2	74.02	0.0813	1792.7
	0.25	62.39	0.0476	842.1
	0.3	50.15	0.0296	486.1
	0.35	37.98	0.0207	365.8
	0.4	26.68	0.0149	276.4
CB	0.2	74.02	0.0703	1103.4
	0.25	62.39	0.0444	646.0
	0.3	51.48	0.0138	360.6
	0.35	37.98	0.0123	334.4
	0.4	26.68	0.0103	251.6

Table 2
The surface-volume ratio of the composite lattice structures.

Model	Strut radius (mm)	Specific surface area (mm^2/mm^3)
AB/BA	0.2	10.03
	0.25	7.74
	0.3	6.17
	0.35	5.02
	0.4	4.12
AC/CA	0.2	9.87
	0.25	7.59
	0.3	6.04
	0.35	4.88
	0.4	3.97
BC/CB	0.2	9.36
	0.25	7.13
	0.3	5.58
	0.35	4.42
	0.4	3.48

FE analysis of uniaxial compressive behaviors was conducted using ANSYS Workbench software to investigate the mechanical properties and visualize the stress distribution of the composite lattice structures. The parameters of material in the FE analysis process were as follows: the density of 4.46 g/cm^3, the elastic modulus of 110 GPa, the Poisson ratio of 0.3, and the compressive yield strength of 830 MPa based on previous study [32]. The 3D linear triangular prism elements (C3D6) were used to mesh the composite lattice structures. In terms of the boundary conditions, the bottom surface was fixed and the compressive stress of 73 MPa was applied on the top surface [33].

2.2. Materials and manufacturing

The hydride-dehydride Ti (HDH-Ti) powder (Beijing Xing Rong Yuan Co., Ltd, China) was used as raw materials. The powder was treated in a ball mill to improve the flowability. The ratio of ball and powder, milling speed, and milling time were 5:1, 200 r/min, and 4h, respectively. The detailed powder characteristic and process parameters were described elsewhere [34–39].

The CP-Ti with optimized composite lattice structures were manufactured by SLM 125HL machine (SLM Solutions GmbH, Lübeck, Germany) under an argon gas atmosphere with O_2 content < 0.05 wt% to reduce oxidation. The process begins with the preparation of CAD files which are subsequently sliced into two-dimensional layers by Materialise Magics [40,41]. The detailed process parameters are as follows based on our previous study [34]: the layer thickness is 30 μm; the scanning speed is 900 mm/s; the laser power is 200 W; the hatching space is 0.14 mm; and the hatching type is a continuous laser mode, which is alternated 33° between each layer. The printing direction is along the direction of the Z-axis.

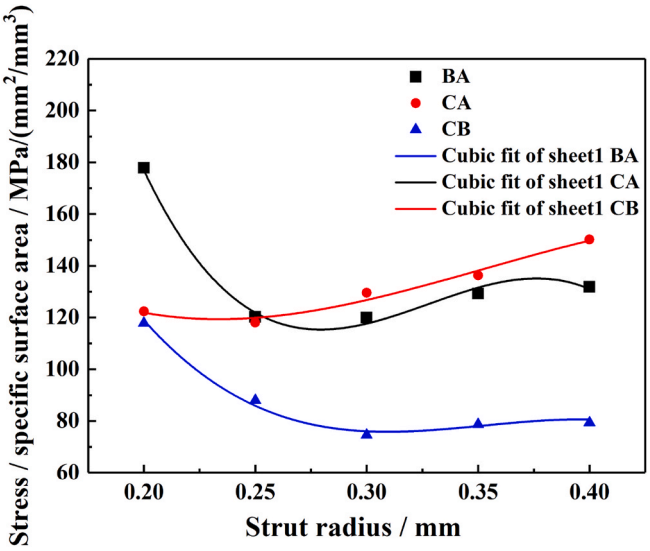

Fig. 5. The variation of stress/specific surface area with the strut radius.

Table 3
Pore sizes of designed BA, CA and CB.

Structures	small pore size (mm)	large pore size (mm)
BA	0.715	2.268
CA	0.518	2.368
CB	0.392	0.692

2.3. Measurement and characterisation

The manufactured specimens were sand-blasted and ultrasonically cleaned in absolute ethyl alcohol and finally dried under vacuum. The relative density was calculated based on the ASTM B962-14 standard [42], and then the porosity was obtained based on Eq. (1). Each specimen was measured five times repeatedly to obtain average results.

$$P = 1 - \frac{m_1 \times \rho_{water}}{(m_3 - m_2) \times \rho_{Ti}} \quad (1)$$

where P is the porosity of specimen, %; m_1 is the mass of the specimen in air, g; ρ_{water} is the density of water, 1 g/cm^3; ρ_{Ti} is the density of solid Ti, 4.507 g/cm^3; m_2 is the mass of the oil-impregnated test specimen in water with the mass of the specimen support tared, g; m_3 is the mass of the oil-impregnated test specimen in air, g.

The scanning electron microscopy (SEM, JSM-6480LV) was used to characterize the morphology. The pore diameter distribution was determined from 50 2D slices images obtained from Solidwords software, and D_{50} is used as average pore size. Based on ISO 13314:2011(E)

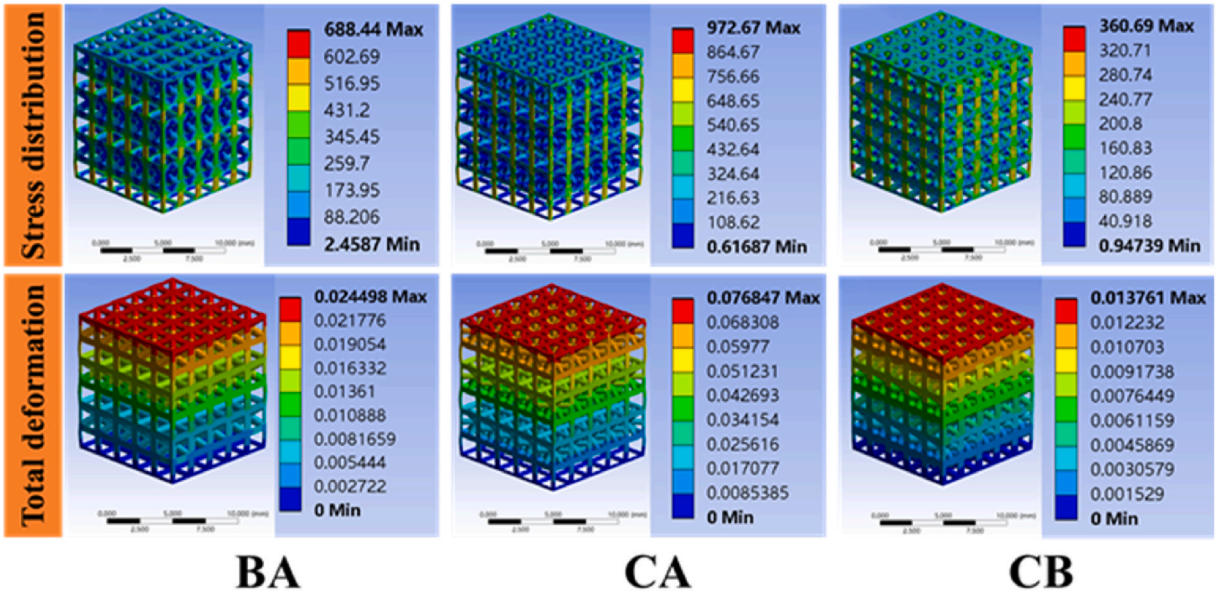

Fig. 6. Von-Mises stress distribution of optimized composite lattice structures: BA with the strut radius of 0.28 mm, CA with the strut radius of 0.23 mm and CB with the strut radius of 0.3 mm.

Table 4
The geometrical parameters and FE results of optimized composite lattice structures.

	BA	CA	CB
Strut radius (mm)	0.28	0.23	0.3
Porosity (%)	71.24	77.12	51.48
Maximum von-Mises stress (MPa)	688.44	972.67	360.69
Maximum total deformation (mm)	0.0244	0.0768	0.0138

[43], uniaxial compressive tests were performed on a universal testing machine (CMT4305) under the compressive strain rate of 0.001 mm/s along the printing direction (Z-axis). For each type of lattice structure, five samples were measured and the average value was calculated.

3. Results and discussion

3.1. FE analysis

Von-Mises stress distribution and total deformation of designed composite lattice structures were firstly analysed by FE to evaluate the strength. Taking the structure with the strut radius of 0.3 mm for example, it can be seen from von-Mises stress distribution (Fig. 3) that the stress is mainly concentrated on the upper surface or the vertical struts. For the AB, AC, and BC structures, the stress is mainly concentrated on the upper surface and the vertical struts of the first, third, and fifth layers (from top to the bottom), while it is mainly concentrated on the vertical struts of the second, fourth, and sixth layers for BA, CA and CB structures. This is mainly related to the internal structure. As shown in Fig. 1, the number of struts in three structures is C > B > A, which leads to structure C has a higher ability to bear loads than structure B and A.

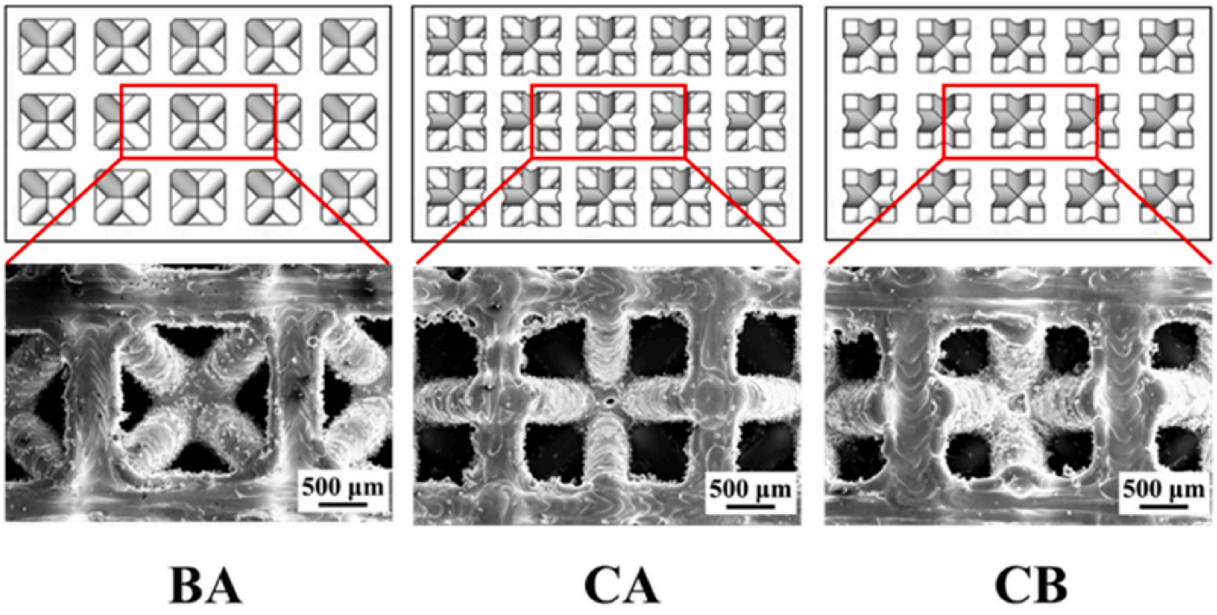

Fig. 7. The SEM images of optimized composite lattice structures BA, CA and CB.

Table 5
Details of manufactured optimized composite strut-based lattices in comparison to designed model.

Model	Design		As-built	
	Porosity (%)	Strut radius (mm)	Porosity (%)	Strut radius (mm)
BA	71.24	0.28	69.68 ± 0.34	0.285 ± 0.002
CA	77.12	0.23	75.3 ± 0.4	0.233 ± 0.002
CB	51.48	0.30	50.11 ± 0.23	0.307 ± 0.004

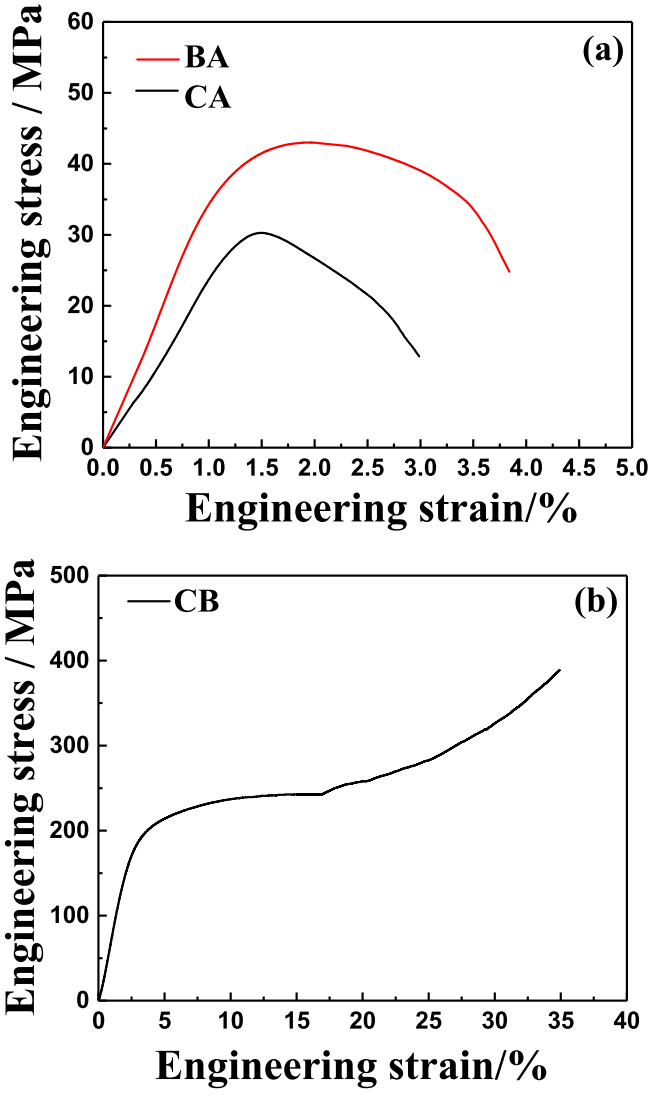

Fig. 8. The compressive stress-strain curves of CP-Ti with optimized composite lattice structures: (a) CP-Ti with BA structure with the strut radius of 0.28 mm and CA structure with the strut radius of 0.23 mm; (b) CP-Ti with CB structure with the strut radius of 0.3 mm.

As a result, the stress is concentrated on the layer composed of A or B unit cell. In addition, it can be seen from Fig. 3 that AB and AC structures exhibit higher maximum von-Mises stress (1454.50 and 1453.90 MPa, respectively) than the other four structures (384.46–782.10 MPa).

The images of the total deformation of six types of structures with a strut radius of 0.3 mm are shown in Fig. 4. It can be seen that the maximum total deformation of AB (0.0701 mm) and AC (0.0708 mm) are higher than the others (0.0138 mm–0.0501 mm). In addition, it can be found that the deformation of AB and AC is uneven which is mainly concentrated on the level struts of the upper layer. In contrast, the deformation of the other four composite lattice structures is relatively uniform. These results are consistent with the results of von-Mises stress distribution.

Table 1 summaries the maximum von-Mises stress and the maximum total deformation of 30 different composite lattice structures designed in this study. It can be seen that the maximum von-Mises stress and the maximum total deformation decrease along with strut radius increasing in the same type structures. In addition, compared with the AB structure, BA structure with the same strut radius and porosity exhibits smaller maximum von-Mises stress and total deformation, indicating that BA structures have higher mechanical properties. As for AC/CA and BC/CB composite lattice structures, similar results are found, namely CA and CB structures exhibit higher mechanical properties than AC and BC structures, respectively. Hence, the BA, CA, and CB structures will be focused on the following studies.

It is well known that the pore features, such as porosity and pore size, can significantly influence the biological properties of implants [44]. In this study, the pore features are directly related to the strut radius. For example, with a larger strut radius, the pore size and the porosity decrease which leads to an increase in the volume and the surface area. However, there is a reduction in specific surface area (Table 2), which is not beneficial for adhesion, proliferation, and differentiation, and the transportation of nutrients [44,45]. Meanwhile, with the larger strut radius, the maximum von-Mises stress becomes smaller, which is beneficial for the mechanical properties. That is to say, a smaller stress/specific surface area would be more desirable for both mechanical and biological properties. Fig. 5 shows the variation of strut radius of BA, CA, and CB structures with stress/specific surface area, and their corresponding fitting curves. It can be seen that the stress/specific surface area of CA and CB structures decreases with the strut radius firstly and then increases. So, the best strut ratios for CA and CB structures are 0.23 and 0.3 mm respectively. As for the BA structure, the stress/specific surface area decreases with the strut radius firstly and then increases, and finally decreases again. However, when the strut radius is higher than 0.4 mm, the porosity becomes too small to be used. Therefore, the best strut radius for the BA structure is 0.28 mm. The pore sizes of three designed BA, CA, and CB structures are listed in Table 3. It can be seen that the small pore size of designed structures is in the range of 400–700 μm, which may be benefit to adhesion, proliferation, and differentiation of cells based on previous studies [46,47]. In addition, the size of the large pores increasing from 700 μm to 2300 μm can be used as a path for the transportation of nutrients and metabolites, and vascularisation.

The mechanical properties of the optimized BA, CA, and CB composite lattice structures were simulated by the FE method. The total deformation and von-Mises stress distribution are shown in Fig. 6, and the FE results together with geometrical parameters are summarised in Table 4. It can be seen from Fig. 6 that the stress distributions within all structures are homogeneous. The maximum stresses for three structures are in the range of 360.69–972.67 MPa (Table 4), which is lower or close to the maximum stress of sample failure in practice [36]. In addition, as can be seen from Table 4, the porosity of all structures is above 50%, which meets the requirements of scaffolds as subchondral bone restorations [48].

3.2. Dimensions and microtopography characterisation

Fig. 7 shows the SEM images and CAD models of the local cross-section of the optimized composite lattice structures. It can be seen that the surface of the lattice structures is rough, which is due to partially melted powders boned on the surfaces of struts and the stair-stepping effect. Comparing the CAD models with the printed samples, it can be found that the geometries of fabricated lattice structures are in line with the CAD models. In addition, there is no macro defects are observed. These results indicate that the printing quality is high.

The detailed morphological parameters of the designed and as-built samples, including the strut radius and porosity are summarised in

Table 6
Comparison of mechanical properties of the CP-Ti with composite lattice structures in this study, trabecular bone, cortical bone, and CP-Ti and Ti–6Al–4V with other structures in literature.

Scaffold	Material	Porosity (%)	Yield strength (MPa)	Compressive modulus (GPa)	Reference
BA	CP-Ti	69.72 ± 0.2	42.28 ± 1.5	4.13 ± 0.11	this study
CA	CP-Ti	75.32 ± 0.35	30.11 ± 0.8	2.61 ± 0.09	this study
CB	CP-Ti	50.15 ± 0.2	176.96 ± 4.2	7.84 ± 0.18	this study
Diamond	CP-Ti	81.12	17.75 ± 0.9	0.586 ± 0.021	[50]
Dodecahedron	CP-Ti	66–81	8.6–36.5	0.58–2.61	[51]
Diamond	Ti–6Al–4V	48.4	156.1 ± 20.3	9.01 ± 0.35	[32]
Step-wise FGPB	Ti–6Al–4V	56.4	170.6 ± 15.6	10.44 ± 0.2	[32]
Diamond	CP-Ti	61.6 ± 0.4	36.2 ± 1.3	0.557 ± 0.006	[52]
Trabecular bone	bone	Up to 90	0.8–11.6	0.022–0.712	[46]
Cortical bone	bone	5–10	10–222	7.7–21.8	[46]

Table 5. It can be seen that all of the as-built strut radius for the BA, CA, and CB composite lattice structures slightly increase (~1.3%~2.3%) and the porosity of as-built structures slightly reduces (~2.1%~2.58%) compared to the designed samples. This is mainly due to the partial melting of some powders surrounding the struts bond to the surfaces of the struts during the SLM process. In addition, the distinct thermal gradient which is caused by the molten and unmolten powders leads to further adhesion of powders to the surfaces of the struts [49].

3.3. Compressive mechanical properties

Fig. 8 shows the compressive stress-strain curves of CP-Ti with optimized BA, CA, and CB structures. All curves exhibit a linear elastic region. Following the linear elastic stage, the curves of CP-Ti with optimized BA and CA composite lattice structures in Fig. 8(a) show that the stress increases nonlinearly with the strain and the slopes of stress-strain curves decrease gradually until the slopes reach zero. After that, the stress-strain curves enter a softening region where the stress declines. Finally, fracture occurred with applied strain after the softening stage. As for the CP-Ti with an optimized CB composite lattice structure, the stress-strain curve (Fig. 8(b)) reaches a relatively long plateau after a linear elastic region and finally is truncated by a densification region with a significant increase in stress.

Table 6 compares the mechanical properties of the CP-Ti with composite lattice structures in this study, trabecular bone, cortical bone, and CP-Ti or Ti–6Al–4V with single lattice structures in literature. The compressive modulus of CP-Ti with composite lattice structures in this study is in the range of 2.61–7.84 GPa and closes to that values of CP-Ti with similar porosity in literature. But the compressive yield strength of CP-Ti with composite lattice structures in this study (30.1–176.96 MPa) is significantly higher than that of CP-Ti with diamond and dodecahedron structures with a similar porosity and close to that of Ti–6Al–4V with diamond structure. Among them, the CP-Ti with CB structure exhibits similar yield strength to the cortical bones (103–222 MPa) while the compressive modulus is also in the range of cortical bones (7.7–21.8 GPa). As a result, CP-Ti with CB structure has the best potential for subchondral bone restorations.

4. Conclusions

In this study, six types of composite lattice structures with different strut radius are designed, and the compressive properties are simulated by the FE method. Based on the simulation results, CP-Ti samples with optimized structures and strut radius are fabricated by SLM, and the microstructure and mechanical properties are characterised. The main conclusions are summarised as follows:

(1) BA, CA, and CB lattice structures exhibit smaller maximum von-Mises stress compared with AB, AC, and BC structures with the same strut radius, indicating that these three structures have higher mechanical properties. The optimized strut radius of BA, CA, and CB structures are 0.28, 0.23, and 0.30 mm respectively.
(2) The strut radius of the SLM-fabricated samples increases slightly while the porosity decreases compared with the designed samples, but the deviations are in a reasonable range. In addition, there are no macro defects observed in the 3D printed samples.
(3) The compressive yield strength and compressive modulus of CP-Ti with BA, CA, and CB structures are in the range of 30.11–176.96 MPa and 2.61–4.13 GPa, respectively. Among them, the CP-Ti with CB composite lattice structure exhibits similar strength and compressive modulus to the cortical bone and therefore can be considered for further study for use as subchondral bone restorations.

Data availability

The data that support the findings of this study are available from the corresponding or first authors on reasonable request.

CRediT authorship contribution statement

Wei Xu: Conceptualization, Data curation, Formal analysis, Writing - original draft, Writing - review & editing. **Aihua Yu:** Data curation, Formal analysis, Investigation. **Xin Lu:** Conceptualization, Data curation, Formal analysis, Writing - original draft, Writing - review & editing, Supervision, Project administration. **Maryam Tamaddon:** Investigation, Writing - review & editing. **Mengdi Wang:** Investigation, Writing - review & editing. **Jiazhen Zhang:** Investigation, Writing - review & editing. **Jianliang Zhang:** Investigation, Writing - review & editing. **Xuanhui Qu:** Investigation, Writing - review & editing. **Chaozong Liu:** Investigation, Writing - review & editing. **Bo Su:** Investigation, Writing - review & editing.

Declaration of competing interest

The authors declare that they have no known competing for financial interests or personal relationships that could have appeared to influence the work reported in this paper.

Acknowledgments

This research work is supported by the National Natural Science Foundation of China (51922004, 51874037), State Key Lab of Advanced Metals and Materials, University of Science and Technology Beijing (2019-Z14), and Fundamental Research Funds for the Central Universities (FRF-TP-19005C1Z). Chaozong Liu acknowledges the support from the European Commission via the H2020 MSCA RISE BAMOS programme (734156). Bo Su would like to thank the financial support from the MRC (MR/S010343/1) and the EU H2020 MSCA RISE Bio-TUNE programme. Wei Xu acknowledges the support from the China Scholarship Council (CSC) for a CSC Ph.D. scholarship (201906460106).

References

[1] D. Bicho, S. Ajami, C.Z. Liu, R.L. Reis, J.M. Oliveira, Peptide-biofunctionalization of biomaterials for osteochondral tissue regeneration in early stage osteoarthritis: challenges and opportunities, J. Mater. Chem. B 7 (2019) 1027–1044.

[2] M. Tamaddon, L. Wang, Z.Y. Liu, C.Z. Liu, Osteochondral tissue repair in osteoarthritic joints: clinical challenges and opportunities in tissue engineering, Bio-design Manuf. 1 (2018) 101–114.

[3] T. Ghassemi, A. Shahroodi, M.H. Ebrahimzadeh, Current concepts in scaffolding for bone tissue engineering, Arch. Bone. Joint. Surg. 6 (2018) 90–99.

[4] V. Karageorgiou, D.L. Kaplan, Porosity of 3D biomaterial scaffolds and osteogenesis, Biomaterials 26 (2005) 5474–5491.

[5] J. Wieding, T. Lindner, P. Bergschmidt, R. Bader, Biomechanical stability of novel mechanically adapted open-porous titanium scaffolds in metatarsal bone defects of sheep, Biomaterials 46 (2015) 35–47.

[6] Z.Y. Chen, X.C. Yan, S. Yin, L.L. Liu, X. Liu, G.R. Zhao, W.Y. Ma, W.Z. Qi, Z.M. Ren, H.L. Liao, M. Liu, D.Z. Cai, H. Fang, Influence of the pore size and porosity of selective laser melted Ti6Al4V ELI porous scaffold on cell proliferation, osteogenesis and bone ingrowth, Mater. Sci. Eng. C 106 (2020), 110289.

[7] S. Ma, Q. Tang, Q.X. Feng, J. Song, X.X. Han, F.Y. Guo, Mechanical behaviours and mass transport properties of bone-mimicking scaffolds consisted of gyroid structures manufactured using selective laser melting, J. Mech. Behav. Biomed. Mater. 93 (2019) 158–169.

[8] L. Zhang, S. Feih, S. Daynes, S. Chang, M.Y. Wang, J. Wei, W.F. Lu, Energy absorption characteristics of metallic triply periodic minimal surface sheet structures under compressive loading, Addit. Manuf. 23 (2018) 505–515.

[9] W.W. Wu, W.X. Hu, G.A. Qian, H.T. Liao, X.Y. Xu, F. Berto, Mechanical design and multifunctional applications of chiral mechanical metamaterials: a review, Mater. Des. 180 (2019), 107959.

[10] R. De Santis, A. Gloria, T. Russo, U. D'Amora, S. Zeppetelli, A. Tampieri, T. Herrmannsdörfer, L. Ambrosio, A route toward the development of 3D magnetic scaffolds with tailored mechanical and morphological properties for hard tissue regeneration: preliminary study, Virtual, Phys. Prototy. 6 (2011) 189–195.

[11] T. Russo, U. D'Amora, A. Gloria, M. Tunesi, M. Sandri, S. Rodilossi, D. Albani, G. Forloni, C. Giordano, A. Cigada, A. Tampieri, R. De Santis, L. Ambrosio, Systematic analysis of injectable materials and 3D rapid prototyped magnetic scaffolds: from CNS applications to soft and hard tissue repair/regeneration, Procedia. Eng. 59 (2013) 233–239.

[12] Y.L. Hao, S.J. Li, R. Yang, Biomedical titanium alloys and their additive manufacturing, Rare Met. 35 (2016) 661–671.

[13] L. Bai, C. Gong, X.H. Chen, Y.X. Sun, J.F. Zhang, L.C. Cai, S.Y. Zhu, S.Q. Xie, Additive manufacturing of customized metallic orthopedic implants: materials, structures, and surface modifications, Metals 9 (2019) 1004.

[14] M. de Wild, R. Schumacher, K. Mayer, E. Schkommodau, D. Thoma, M. Bredell, A. Kruse Gujer, K.W. Grätz, F.E. Weber, Bone regeneration by the osteoconductivity of porous titanium implants manufactured by selective laser melting: a histological and micro computed tomography study in the rabbit, Tissue Eng. 19 (2013) 2645–2654.

[15] D. Barba, E. Alabort, R.C. Reed, Synthetic bone: design by additive manufacturing, Acta Biomater. 97 (2019) 637–656.

[16] M.Y. Zhang, Z.Y. Yang, Z.X. Lu, B.H. Liao, X.F. He, Effective elastic properties and initial yield surfaces of two 3D lattice structures, Int. J. Mech. Sci. 138–139 (2018) 146–158.

[17] S.M. Ahmadi, S.A. Yavari, R. Wauthle, B. Pouran, J. Schrooten, H. Weinans, A. A. Zadpoor, Additively manufactured open-cell porous biomaterials made from six different space-filling unit cells: the mechanical and morphological properties, Materials 8 (2015) 1871–1896.

[18] F. Liu, Z.F. Mao, P. Zhang, D.Z. Zhang, J.J. Jiang, Z.B. Ma, Functionally graded porous scaffolds in multiple patterns: new design method, physical and mechanical properties, Mater. Des. 160 (2018) 849–860.

[19] H. Wang, K.X. Su, L.Z. Su, P.P. Liang, P. Ji, C. Wang, The effect of 3D-printed Ti6Al4V scaffolds with various macropore structures on osteointegration and osteogenesis: a biomechanical evaluation, J. Mech. Behav. Biomed. Mater. 88 (2018) 488–496.

[20] A. Ataee, Y. Li, M. Brandt, C.E. Wen, Ultrahigh-strength titanium gyroid scaffolds manufactured by selective laser melting (SLM) for bone implant applications, Acta Mater. 158 (2018) 354–368.

[21] F.S.L. Bobbert, K. Lietaert, A.A. Eftekhari, B. Pouran, S.M. Ahmadi, H. Weinans, A. A. Zadpoor, Additively manufactured metallic porous biomaterials based on minimal surfaces: a unique combination of topological, mechanical, and mass transport properties, Acta Biomater. 53 (2017) 572–584.

[22] Y. Du, H.X. Liang, D.Q. Xie, N. Mao, J.F. Zhao, Z.J. Tian, C.J. Wang, L.D. Shen, Finite element analysis of mechanical behavior, permeability of irregular porous scaffolds and lattice-based porous scaffolds, Mater. Res. Express 6 (2019), 105407.

[23] H.A. Zaharin, A.M. AbdulRani, F.I. Azam, T.L. Ginta, N. Sallih, A. Ahmad, N. A. Yunus, T.Z.A. Zulkifli, Effect of unit cell type and pore size on porosity and mechanical behavior of additively manufactured Ti6Al4V scaffolds, Materials 12 (2018), 2402.

[24] W. Xu, X. Lu, B. Zhang, C.C. Liu, S.M. Lv, S.D. Yang, X.H. Qu, Effects of porosity on mechanical properties and corrosion resistances of PM-fabricated porous Ti-10Mo alloy, Metals 8 (2018) 188–201.

[25] W. Xu, M. Li, C.E. Wen, S.M. Lv, C.C. Liu, X. Lu, X.H. Qu, The mechanical properties and in vitro biocompatibility of PM-fabricated Ti-28Nb-35.4Zr alloy for orthopedic implant applications, Materials 11 (2018) 531–543.

[26] W. Xu, X. Lu, M.D. Hayat, J.J. Tian, C. Huang, M. Chen, X.H. Qu, C.E. Wen, Fabrication and properties of newly developed Ti35Zr28Nb scaffolds fabricated by powder metallurgy for bone-tissue engineering, J. Mater. Res. Technol. 8 (2019) 3696–3704.

[27] W. Xu, J.J. Tian, Z. Liu, X. Lu, M.D. Hayat, Y. Yan, Z. Li, X.H. Qu, C.E. Wen, Novel porous Ti35Zr28Nb scaffolds fabricated by powder metallurgy with excellent osteointegration ability for bone-tissue engineering applications, Mater. Sci. Eng. C 105 (2019), 110015.

[28] N. Sudarmadji, J.Y. Tan, K.F. Leong, C.K. Chua, Y.T. Loh, Investigation of the mechanical properties and porosity relationships in selective laser-sintered polyhedral for functionally graded scaffolds, Acta Biomater. 7 (2011) 530–537.

[29] S.Y. Choy, C. Sun, K.F. Leong, J. Wei, Compressive properties of functionally graded lattice structures manufactured by selective laser melting, Mater. Des. 131 (2017) 112–120.

[30] X.Y. Zhang, G. Fang, S. Leeflang, A.A. Zadpoor, J. Zhou, Topological design, permeability and mechanical behavior of additively manufactured functionally graded porous metallic biomaterials, Acta Biomater. 84 (2019) 437–452.

[31] L. Yang, R. Mertens, M. Ferrucci, C.Z. Yan, Y.S. Shi, S.F. Yang, Continuous graded Gyroid cellular structures fabricated by selective laser melting: design, manufacturing and mechanical properties, Mater. Des. 162 (2019) 394–404.

[32] J.P. Shi, J.Q. Yang, Z.A. Li, L.Y. Zhu, L. Li, X.S. Wang, Design and fabrication of graduated porous Ti-based alloy implants for biomedical applications, J. Alloys Compd. 728 (2017) 1043–1048.

[33] Y.M. Diao, Biomechanics: Principles and Applications, Tongji University Press, 1991, pp. 216–218.

[34] W. Xu, S.Q. Xiao, X. Lu, G. Chen, C.C. Liu, X.H. Qu, Fabrication of commercial pure Ti by selective laser melting using hydride-dehydride titanium powders treated by ball milling, J. Mater. Sci. Technol. 35 (2019) 322–327.

[35] W. Xu, A.H. Yu, X. Lu, M. Tamaddon, L.Q. Ng, M.D. Hayat, M.D. Wang, J.L. Zhang, X.H. Qu, C.Z. Liu, Synergistic interactions between wear and corrosion of Ti-16Mo orthopedic alloy, J. Mater. Res. Technol. 9 (5) (2020) 9996–10003.

[36] W. Xu, C.J. Hou, Y.X. Mao, L. Yang, M. Tamaddon, J.L. Zhang, X.H. Qu, C.Z. Liu, B. Su, X. Lu, Characteristics of novel Ti-10Mo-xCu alloy by powder metallurgy for potential biomedical implant applications, Bioact. Mater. 5 (3) (2020) 659–666.

[37] W. Xu, X. Lu, L.N. Wang, Z.M. Shi, S.M. Lv, Q. Ma, X.H. Qu, Mechanical properties, in vitro corrosion resistance and biocompatibility of metal injection molded Ti-12Mo alloy for dental applications, J. Mech. Behav. Biomed. 88 (2018) 534–547.

[38] W. Xu, M. Chen, X. Lu, D.W. Zhang, H.P. Singh, J.S. Yu, Y. Pan, X.H. Qu, C.Z. Liu, Effect of Mo content on corrosion and tribocorrosion behaviours of Ti-Mo orthopaedic alloys fabricated by powder metallurgy, Corrosion Sci. 168 (2020), 108557.

[39] W. Xu, X. Lu, J.J. Tian, C. Huang, M. Chen, Y. Yan, L.N. Wang, X.H. Qu, C.E. Wen, Microstructure, wear resistance, and corrosion performance of Ti35Zr28Nb alloy fabricated by powder metallurgy for orthopedic applications, J. Mater. Sci. Technol. 41 (2020) 191–198.

[40] S.L. Sing, W.Y. Yeong, Laser powder bed fusion for metal additive manufacturing: perspectives on recent developments, Virtual, Phys. Prototy. 15 (2020) 359–370.

[41] R.P. Shi, S.A. Khairallah, T.T. Roehling, T.W. Heo, J.T. Mckeown, M.J. Matthews, Microstructural control in metal laser powder bed fusion additive manufacturing using laser beam shaping strategy, Acta Mater. 184 (2020) 284–305.

[42] ASTM B962-14, Standard Test Methods for Density of Compacted or Sintered Powder Metallurgy PM Products Using Archimedes' Principle, 2017.

[43] ISO 13314, Mechanical Testing of Metals-Ductility Testing-Compression Test for Porous and Cellular Metals, 2011.

[44] W. Xu, Z. Liu, X. Lu, J.J. Tian, G. Chen, B.W. Liu, Z. Li, X.H. Qu, C.E. Wen, Porous Ti-10Mo alloy fabricated by powder metallurgy for promoting bone regeneration, Sci. China Mater. 62 (2019) 1053–1064.

[45] X.J. Wang, S.Q. Xu, S.W. Zhou, W. Xu, M. Leary, P. Choong, M. Qian, M. Brandt, Y. M. Xie, Topological design and additive manufacturing of porous metals for bone scaffolds and orthopaedic implants: a review, Biomaterials 83 (2016) 127–141.

[46] D. Barba, E. Alabort, R.C. Reed, Synthetic bone: design by additive manufacturing, Acta Biomater. 97 (2019) 637–656.

[47] Goats M.C. Kruyt, J.D. de Bruijn, C.E. Wilson, F.C. Oner, C.A. van Blitterswijk, A. J. Verbout, W.J.A. Dhert, Viable osteogenic cells are obligatory for tissue-engineered ectopic bone formation in goats, Tissue Eng. 9 (2) (2003) 327–336.

[48] S. Van Bael, G. Kerckhofs, M. Moesen, G. Pyka, J. Schrooten, J.P. Kruth, Micro-CT-based improvement of geometrical and mechanical controllability of selective laser melted Ti6Al4V porous structures, Mater. Sci. Eng. A 528 (2011) 7423–7431.

[49] C.Z. Yan, L. Hao, A. Hussein, P. Young, Ti-6Al-4V triply periodic minimal surface structures for bone implants fabricated via selective laser melting, J. Mach. Behave. Biomed. Mater. 51 (2015) 61–73.

[50] C.J. Han, Y. Li, Q. Wang, S.F. Wen, Q.S. Wei, C.Z. Yan, L. Hao, J. Liu, Y.S. Shi, Continuous functionally graded porous titanium scaffolds manufactured by selective laser melting for bone implants, J. Mech. Behave. Biomed. Mater. 80 (2018) 119–127.

[51] R. Wauthle, S.M. Ahmadi, S. Amin, M. Mulier, A.A. Zadpoor, H. Weinans, J. Van Humbeeck, J.-P. Kruth, J. Schrooten, Revival of pure titanium for dynamically loaded porous implants using additive manufacturing, Mater. Sci. Eng. C 54 (2015) 94–100.

[52] T. Naoya, F. Shunsuke, T. Mitsuru, S. Kiyoyuki, O. Bungo, N. Takashi, M. Tomiharu, K. Tadashi, M. Shuichi, Effect of pore size on bone ingrowth into porous titanium implants fabricated by additive manufacturing: an in vivo experiment, Mater. Sci. Eng. C 59 (2016) 690–701.